Supplementary Information of "Insights on Ozone Formation Sensitivity in Southeast and East Asian Megacities during ASIA-AQ"

Cho et al.

Correspondence to: Alessandro Franchin (franchin@ucar.edu)

Table S1. Summary of DC-8 research flights.

Location	Flight number	Flight date	Take-off time (LT)	Landing time (LT)
Philippines	RF01	2024-02-06	09:42	18:05
	RF02	2024-02-07	09:05	16:57
	RF03	2024-02-11	08:59	16:43
	RF04	2024-02-15	09:08	17:22
Thailand	RF12	2024-03-16	10:09	17:58
	RF13	2024-03-18	08:25	16:35
	RF14	2024-03-21	08:11	16:09
	RF15	2024-03-25	08:03	15:55
Taiwan	RF05	2024-02-15	10:46[a]	15:14[a]
	RF11	2024-03-13	10:27[a]	13:03[a]
	RF16	2024-03-27	11:11[a]	14:00[a]
South Korea	RF06	2024-02-17	10:55	18:17
	RF07	2024-02-26	10:57	18:25
	RF08	2024-03-08	10:19	18:47
	RF09	2024-03-10	12:13	18:51
	RF10	2024-03-11	10:14	18:48

[a] For Taiwan flights, the listed times correspond to the DC-8 sampling time over Taiwan rather than the full flight duration.

Table S2. Instrumentation details for data used in this study.

Species	Instrument (Method)	Reference
Photolysis frequencies	CAFS (Charged-coupled device actinic spectroradiometers)	Hall et al. (2018)
Meteorological parameters	MMS (Meteorological measurement system)	Gaines et al. (1992)
H_2O	DLH (Diode laser hygrometer)	Diskin et al. (2002)
CO, CH_4	DACOM (Diode laser spectrometer)	Sachse et al. (1987)
NO, NO_2[a]	NO_xO_3 (Chemiluminescence)	Ridley and Grahek (1990)
	CANOE (Cavity enhanced absorption spectrometry)	Bailey et al. (2024)
O_3[b]	NO_xO_3 (Chemiluminescence)	Ridley et al. (1992)
	ROZE (Cavity-enhanced UV absorption)	Hannun et al. (2020)
HCHO	ISAF (Laser-induced fluorescence)	Cazorla et al. (2015)
PANs	GT-TD-CIMS (Thermal dissociation chemical ionization mass spectrometry using I^- reagent ion)	Lee et al. (2020)
CHOCHO	CAESAR (Cavity enhanced absorption spectroscopy)	Min et al. (2016)
HNO_3, HCN, H_2O_2	CIT-CIMS (Chemical ionization mass spectrometry using CF_3O^- reagent ion)	Crounse et al. (2006)
VOCs[c]	TOGA-TOF (Online gas chromatography with time-of-flight mass spectrometry)	Apel et al. (2015); Jeong et al. (2025)
	WAS (Whole air sampler)	Simpson et al. (2020)
	PTR-ToF-MS (Proton-transfer-reaction time-of-flight mass spectrometry)	Reinecke et al. (2023)

[a] The primary NO_2 dataset is from NO_xO_3. Periods with calibration or instrument downtime were gap-filled with CANOE.
[b] Primary dataset depends on deployment: NO_xO_3 for Metro Manila (MM); ROZE for Bangkok Metropolitan Region (BMR), Tainan-Kaohsiung Metropolitan Area (TKMA), and Seoul Metropolitan Area (SMA). Occasional gaps were filled using the alternate instrument.
[c] Alkanes, alkenes, and aromatics were taken primarily from WAS. TOGA-TOF provided biogenic VOCs (BVOCs) and oxidized VOCs (OVOCs). PTR-ToF-MS (selected aromatics and BVOCs) was used when both WAS and TOGA data were unavailable.

S1 Average VOC reactivity speciation

VOC reactivity (VOCR) is defined as the sum of the reaction rate coefficients between OH and each measured VOC species ($k_{\mathrm{OH+VOC}_i}$), weighted by the concentration of that species ([VOC_i]):

$$\mathrm{VOCR} = \Sigma k_{\mathrm{OH+VOC}_i}[\mathrm{VOC}_i] \quad \text{(S1)}$$

In Figs. S1–S4, VOC shortform names are from Master Chemical Mechanism (MCMv3.3.1; available at: https://www.mcm.york.ac.uk/MCM).

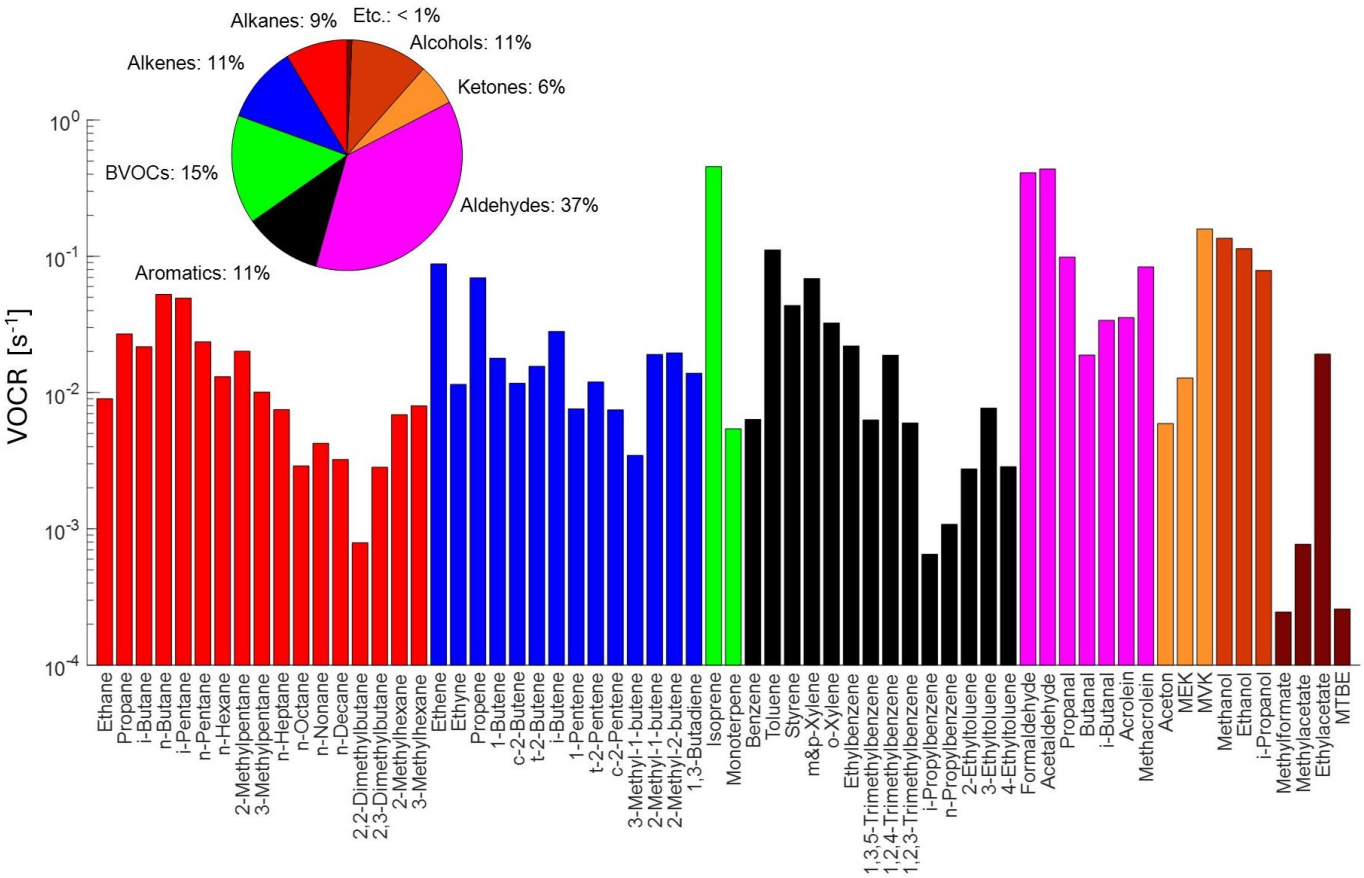

Figure S1. Contribution of individual VOC species to VOC reactivity (VOCR) measured in Metro Manila (MM) below 750 m above sea level (asl). The pie chart summarizes the average fractional contributions of VOC classes to VOCR.

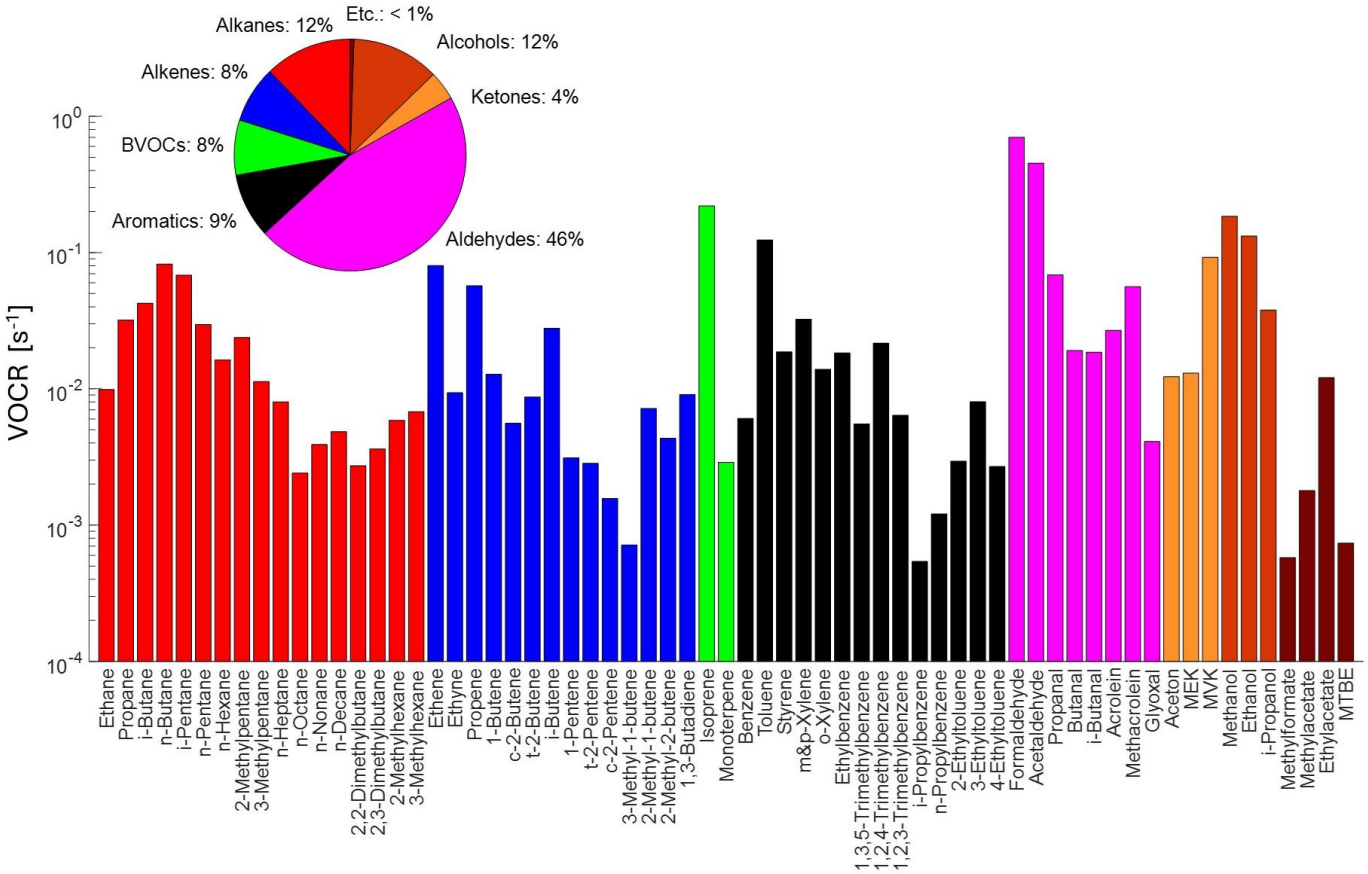

Figure S2. Contribution of individual VOC species to VOCR measured in Bangkok Metropolitan Region (BMR) below 750 m asl. The pie chart summarizes the average fractional contributions of VOC classes to VOCR.

30

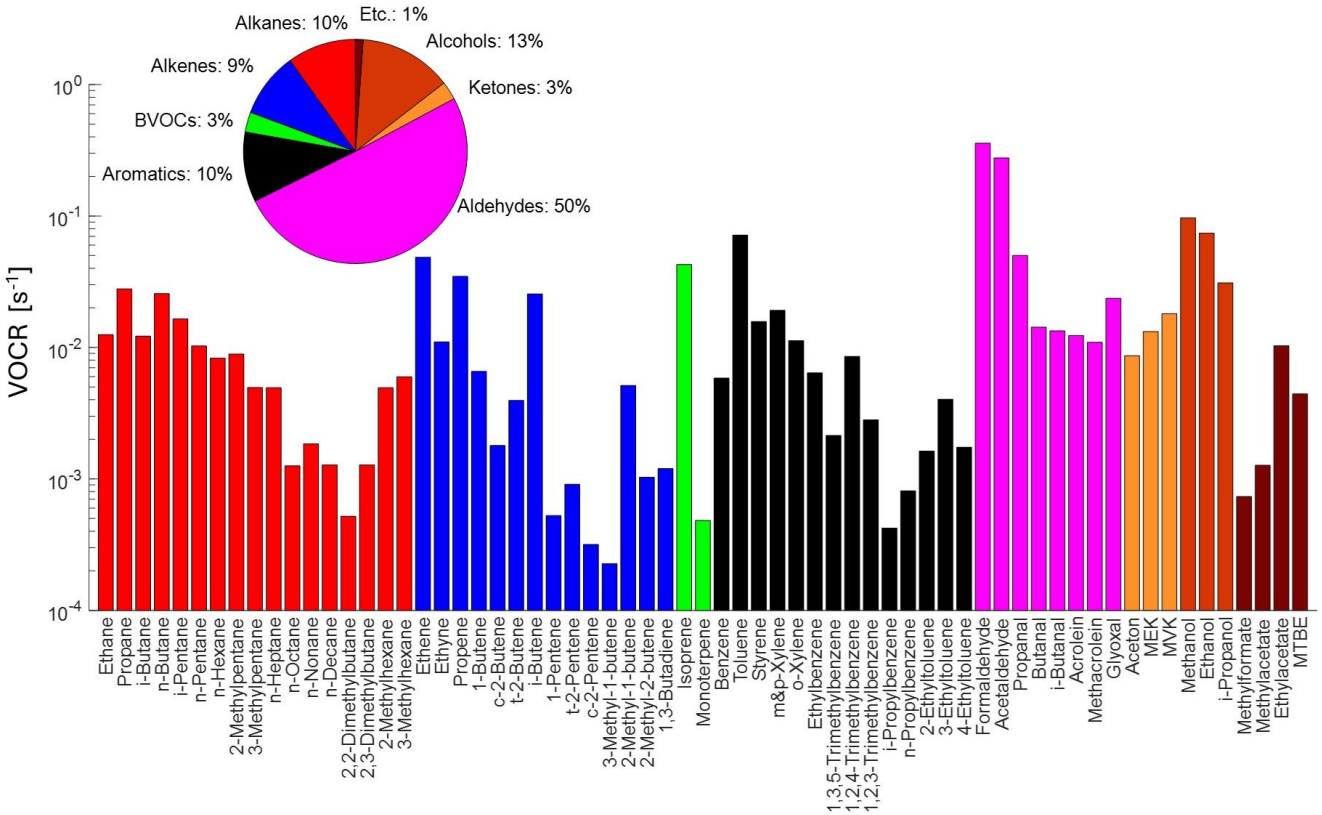

Figure S3. Contribution of individual VOC species to VOCR measured in Tainan-Kaohsiung Metropolitan Area (TKMA) below 750 m asl. The pie chart summarizes the average fractional contributions of VOC classes to VOCR.

35

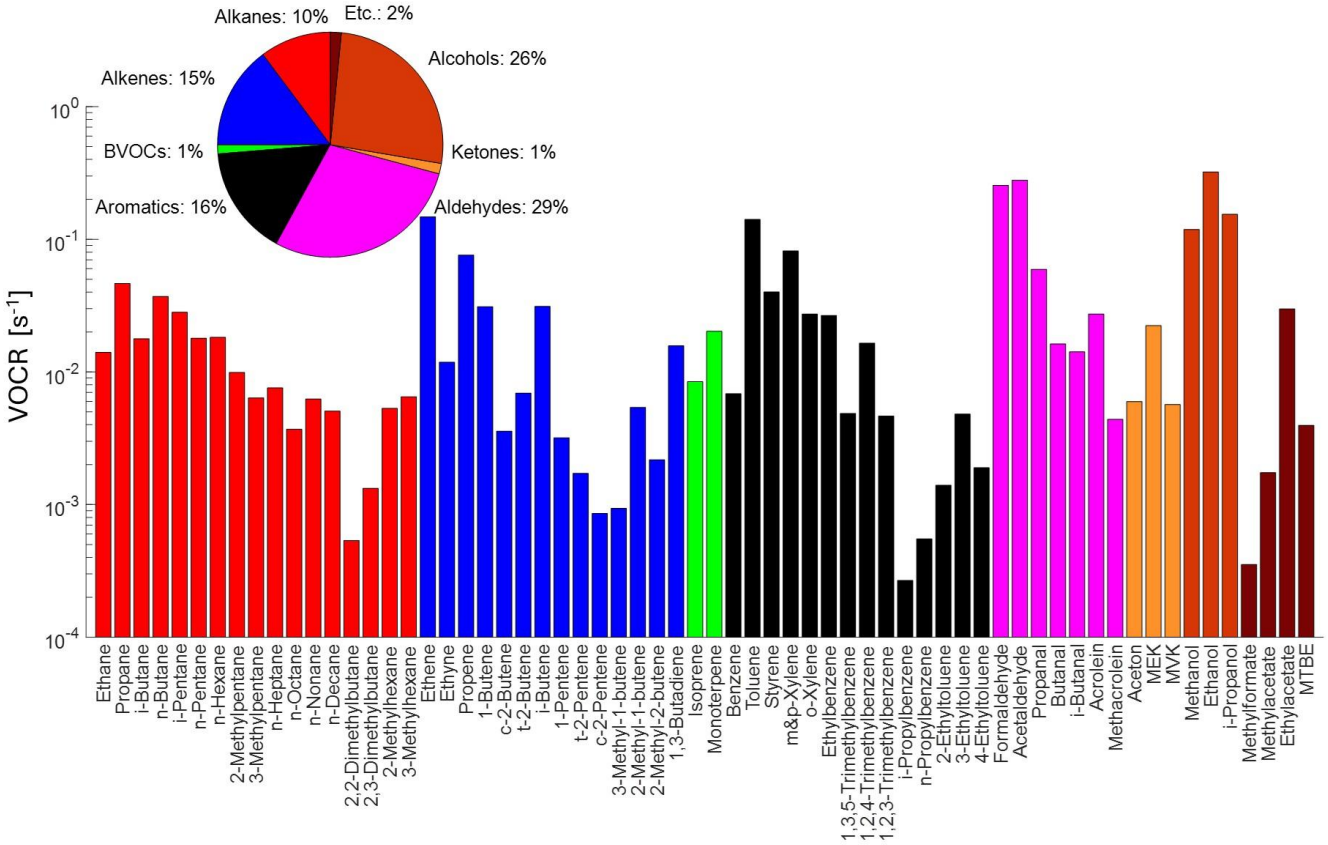

Figure S4. Contribution of individual VOC species to VOCR measured in Seoul Metropolitan Area (SMA) below 750 m asl. The pie chart summarizes the average fractional contributions of VOC classes to VOCR.

S2 Flight steady-state (FSS) box model

To assess the representativeness of the isopleth-derived PO_x, we compared it with PO_x calculated from the flight steady-state (FSS) box model described in previous airborne studies (Crawford et al., 1999; Olson et al., 2006; Schroeder et al., 2020; Kim et al., 2022; Brune et al., 2022; Nault et al., 2024). The FSS model simulates instantaneous photochemical conditions for each observation point with the same model setup as described in Sect. 2.2, while the isopleth framework represents a generalized chemical environment by averaging precursor mixing ratios within each flight track and applying systematic NO_x and VOC scaling factors (Sect. 2.3).

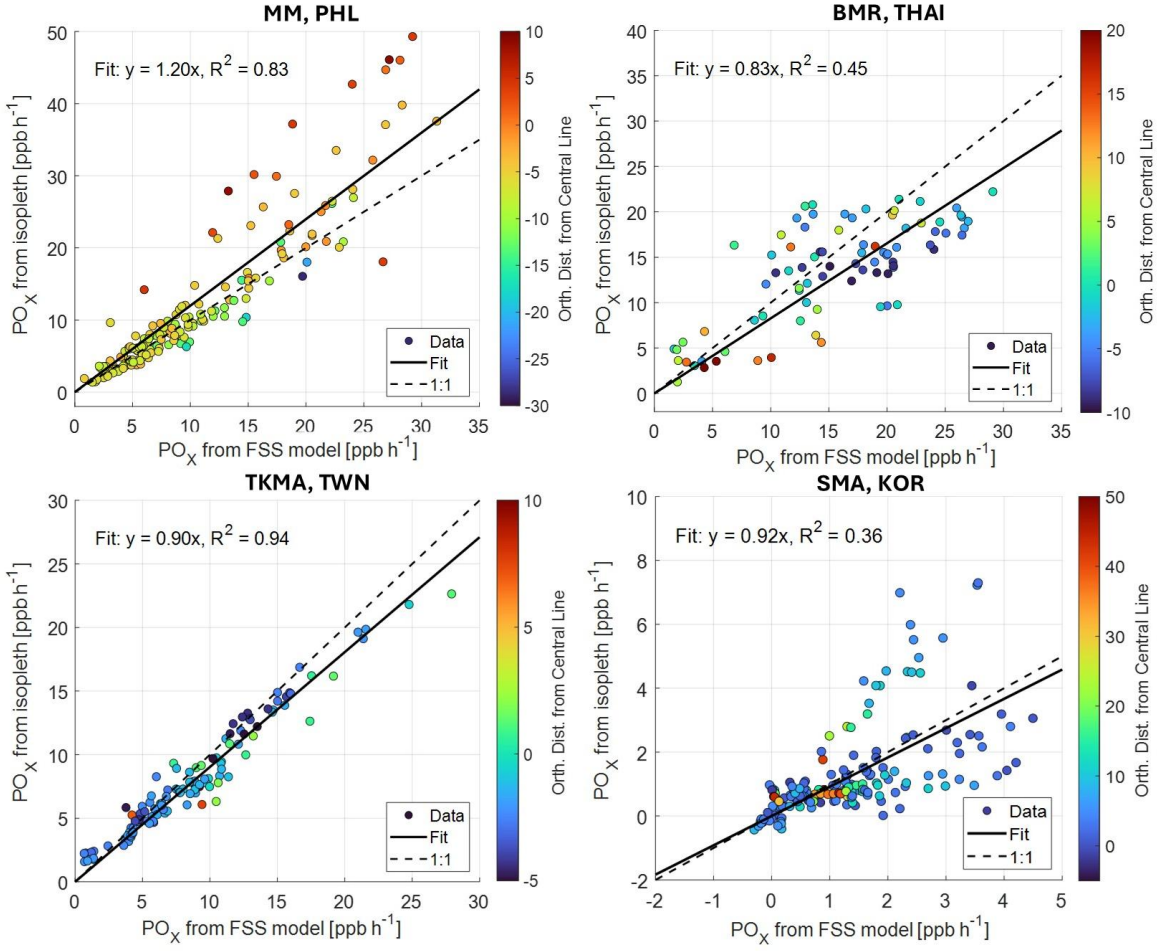

Figure S5. Comparisons between PO_x derived from the isopleth-based approach and the flight steady-state (FSS) box model for four megacities during ASIA-AQ. Colors indicate orthogonal distance from the central transition line (negative: NO_x-sensitive; positive: VOC-sensitive). Solid and dashed lines show the linear fit and 1:1 reference, respectively.

The comparison therefore highlights how regional generalization influences the magnitude and variability of PO_x relative to point-specific calculations. Overall, strong linear relationships with generally good agreement (within 20%) were obtained in MM, BMR, and TKMA (r^2 = 0.45–0.94), indicating that the isopleth approach captures the principal PO_x features

derived from the more discrete FSS model. In MM, data points within the VOC-sensitive regime showed a tendency toward positive bias relative to the FSS simulations. This behavior likely reflects the assumption of fixed VOC speciation during uniform VOC scaling, which can result in a stronger influence on PO_x variability in VOC-sensitive conditions. However, in SMA, the correlation was weaker (r^2 = 0.36), mainly influenced by several high-bias points from one flight (RF06, Tracks 1 and 2) that showed the largest dynamic range of PO_x in the isopleth (Fig. S8), accompanied by elevated photolysis frequency of NO_2 (jNO_2) nearly twice as high as those in other research flights (RF06 average: 0.0071 ± 0.0015 s^{-1}; other RFs average: 0.0040 ± 0.0028 s^{-1}). Under these conditions, the isopleth-based PO_x showed a larger dynamic range (1–7 ppbv h^{-1}) than the point-specific steady-state estimates (1–3.5 ppbv h^{-1}), indicating that the generalized NO_x and VOC scaling can amplify variability rather than smoothing it.

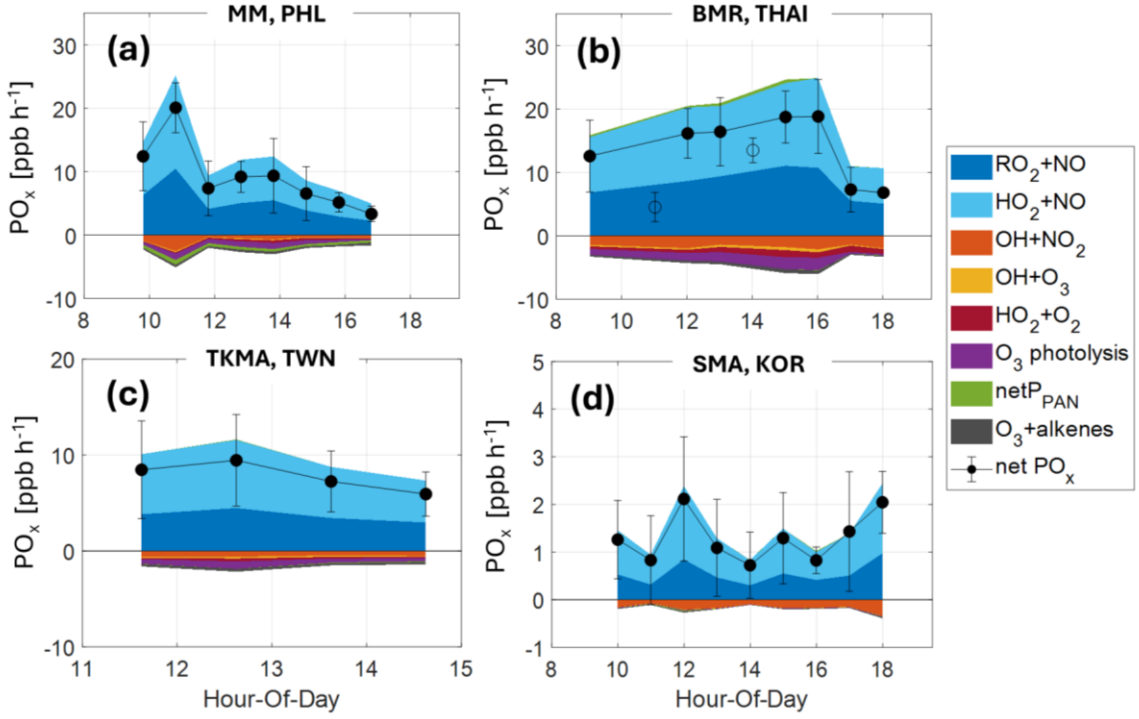

Figure S6. PO_x budget from FSS box model for four megacities during ASIA-AQ. Colored stacked areas represent the individual terms in Eq. 1. Black dots with error bars show the net PO_x (hourly means ± standard deviations). Open dots in BMR indicate data points sampled at relatively higher altitudes (same as Figs. 3 and 5(b)). All times are local time (LT).

The FSS box model is also used to diagnose the PO_x budget as it provides instantaneous production and destruction rates of each term to contribute to net PO_x in Eq. (1). Figure S6 displays the diurnal trends of O_x production and loss terms and resulting net PO_x in each city. Across all cities, O_x production is approximately evenly split between RO_2+NO and HO_2+NO. Loss terms are smaller than productions, dominated by OH+NO_2 and O_3 photolysis (except for SMA due to low solar irradiance), with minor contributions from O_3+alkenes, OH+O_3, and HO_2+O_2. Net PAN production term ($netP_{PAN}$) can act as either a source or a sink of PO_x. In BMR, $netP_{PAN}$ is positive, likely reflecting elevated PAN mixing ratios (2.7 ± 1.5

ppbv) during the biomass-burning period and faster thermal decomposition under warmer conditions, which returns NO_2. In MM and TKMA, negative contributions of $netP_{PAN}$ to PO_x suggests the PAN formation dominates. Lastly, in SMA, colder conditions limit thermal decomposition of PAN, therefore the PAN term is in the loss. However, overall contributions of $netP_{PAN}$ to PO_x are small in all locations (< 2%).

S3 Individual isopleths

S3.1 Metro Manila (MM), Philippines

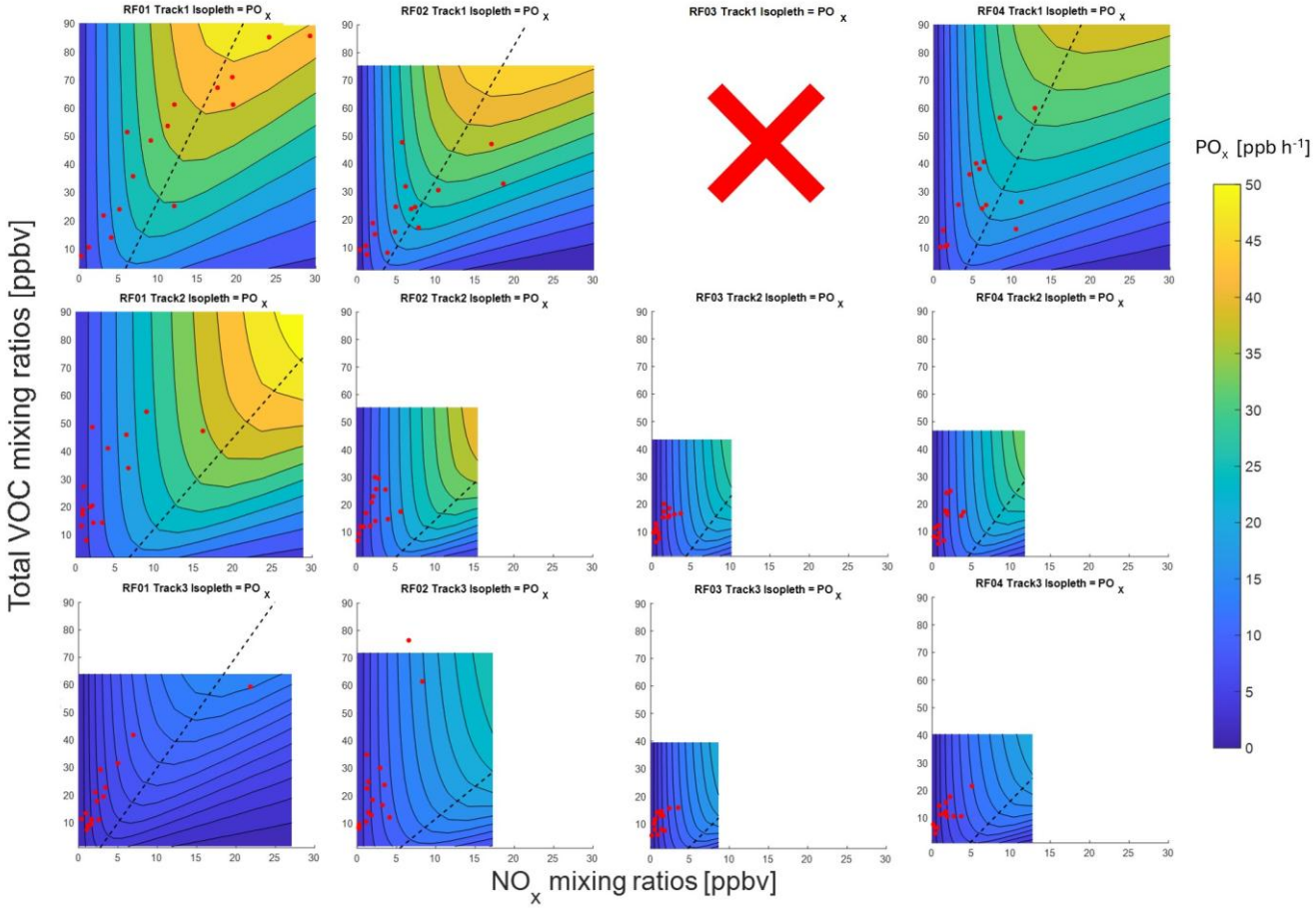

Figure S7. PO_x isopleths for MM. Plot format follows Fig. 4a in the main manuscript. RF03 Track1 is not available due to missing data.

Four DC-8 research flights (RF01–RF04; Table S1) were performed over the Philippines. Figure S7 presents PO_x isopleths for Metro Manila, categorized by research flight and local time: Track 1 (09:00–11:00), Track 2 (11:00–14:00), and Track 3 (14:00–17:00). Data for RF03 Track 1 are excluded due to missing NO_x measurements caused by a temporary instrument failure.

S3.2 Bangkok Metropolitan Region (BMR), Thailand

Four DC-8 research flights (RF12–RF15; Table S1) were performed over Thailand. Figure S8 presents PO_x isopleths for BMR, categorized by research flight and local time: Track 1 (09:00–13:00) and Track 2 (13:00–18:00).

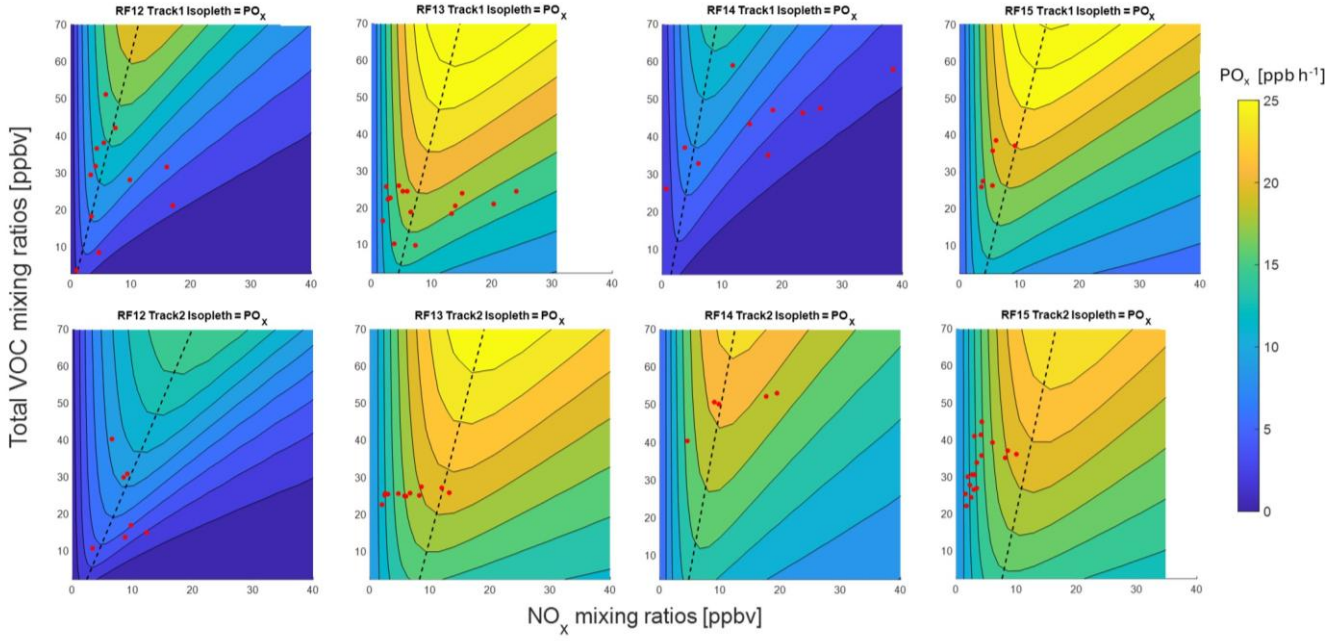

Figure S8. PO_x isopleths for BMR. Plot format follows Fig. 5a in the main manuscript.

S3.3 Tainan-Kaohsiung Metropolitan Area (TKMA), Taiwan

Three DC-8 research flights (RF05, RF11, RF16; Table S1) were performed over Taiwan. Figure S9 presents PO_x isopleths for BMR, categorized by research flight and local time: Track 1 (11:00–13:00) and Track 2 (13:00–15:00).

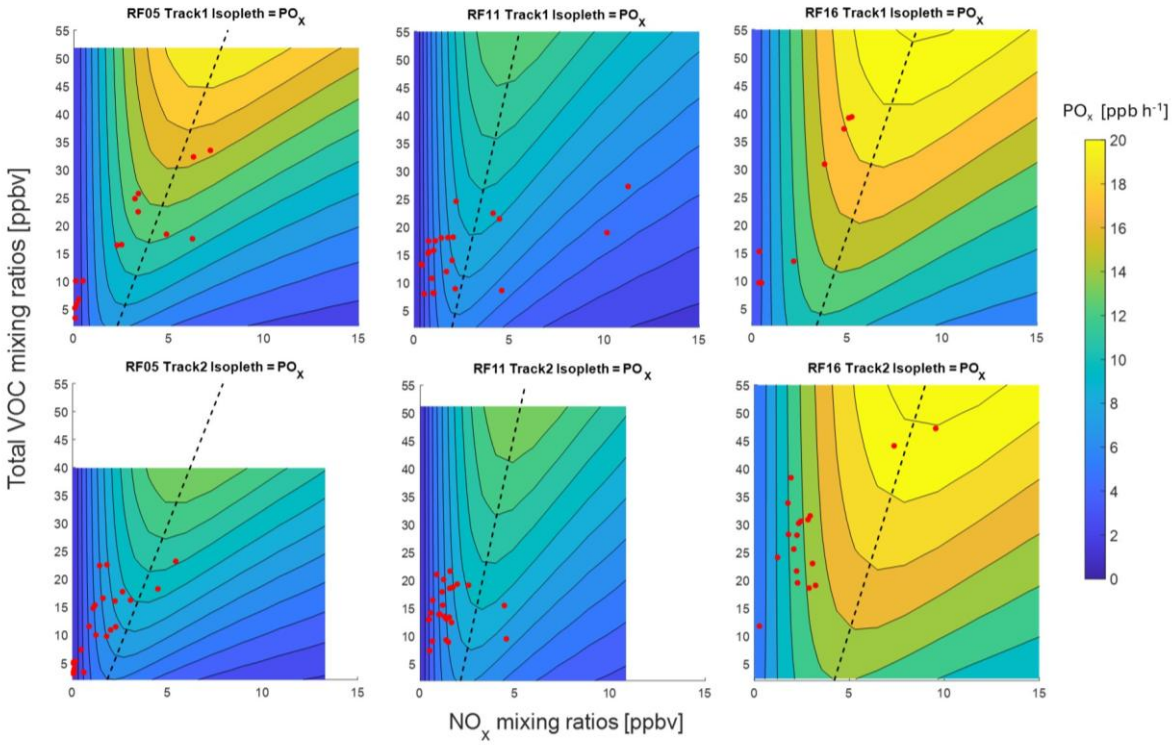

Figure S9. PO_x isopleths for TKMA. Plot format follows Fig. 6a in the main manuscript.

S3.4 Seoul Metropolitan Area (SMA), South Korea

Five DC-8 research flights (RF06–RF10; Table S1) were performed over South Korea. Figure S10 presents PO_x isopleths for SMA, categorized by research flight and local time: Track 1 (10:00–13:00), Track 2 (13:00–16:00), and Track 3 (16:00–19:00). Note that the *x*-axis (NO_x mixing ratios) is shown on a logarithmic scale to better visualize isopleths.

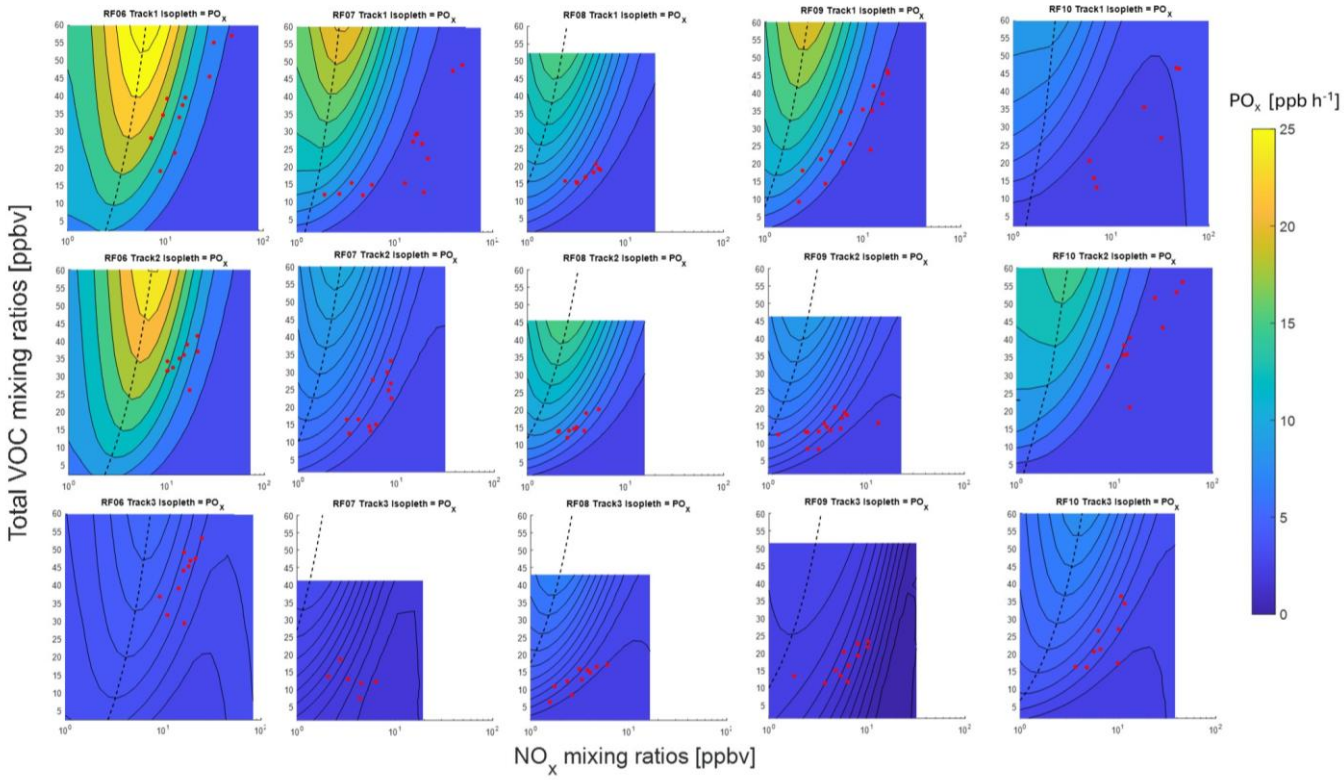

Figure S10. PO_x isopleths for SMA. Plot format follows Fig. 7a in the main manuscript. The *x* axis is in a logarithmic scale.

Table S3. Slopes of the PO_x transition line (ridges of maximum PO_x) from isopleths by city, flight, and track.

City	Flight	Track	Slope	City	Flight	Track	Slope
MM, PHL	RF01	1	5.83	**BMR, THAI**	RF12	1	6.58
	RF01	2	3.25		RF12	2	3.86
	RF01	3	4.01		RF13	1	6.62
	RF02	1	4.85		RF13	2	6.26
	RF02	2	2.70		RF14	1	8.81
	RF02	3	2.33		RF14	2	8.64
	RF03	2	3.83		RF15	1	6.61
	RF03	3	2.81		RF15	2	7.55
	RF04	1	5.97		**RF12–15**	**all**	**7.01**
	RF04	2	3.82	**SMA, KOR**	RF06	1	14.97
	RF04	3	2.95		RF06	2	12.26
	RF01–04	**all**	**4.71**		RF06	3	12.40
TKMA, TWN	RF05	1	9.10		RF07	1	39.99
	RF05	2	8.70		RF07	2	29.15
	RF11	1	14.91		RF07	3	40.07
	RF11	2	15.58		RF08	1	29.45
	RF16	1	10.05		RF08	2	21.07
	RF16	2	11.05		RF08	3	26.07
	RF05, 11, 16	**all**	**11.24**		RF09	1	30.07
					RF09	2	22.18
					RF09	3	20.83
					RF10	1	44.01
					RF10	2	27.14
					RF10	3	16.20
					RF06–10	**all**	**30.27**

S4 Average vertical distributions of PO_x sensitivity

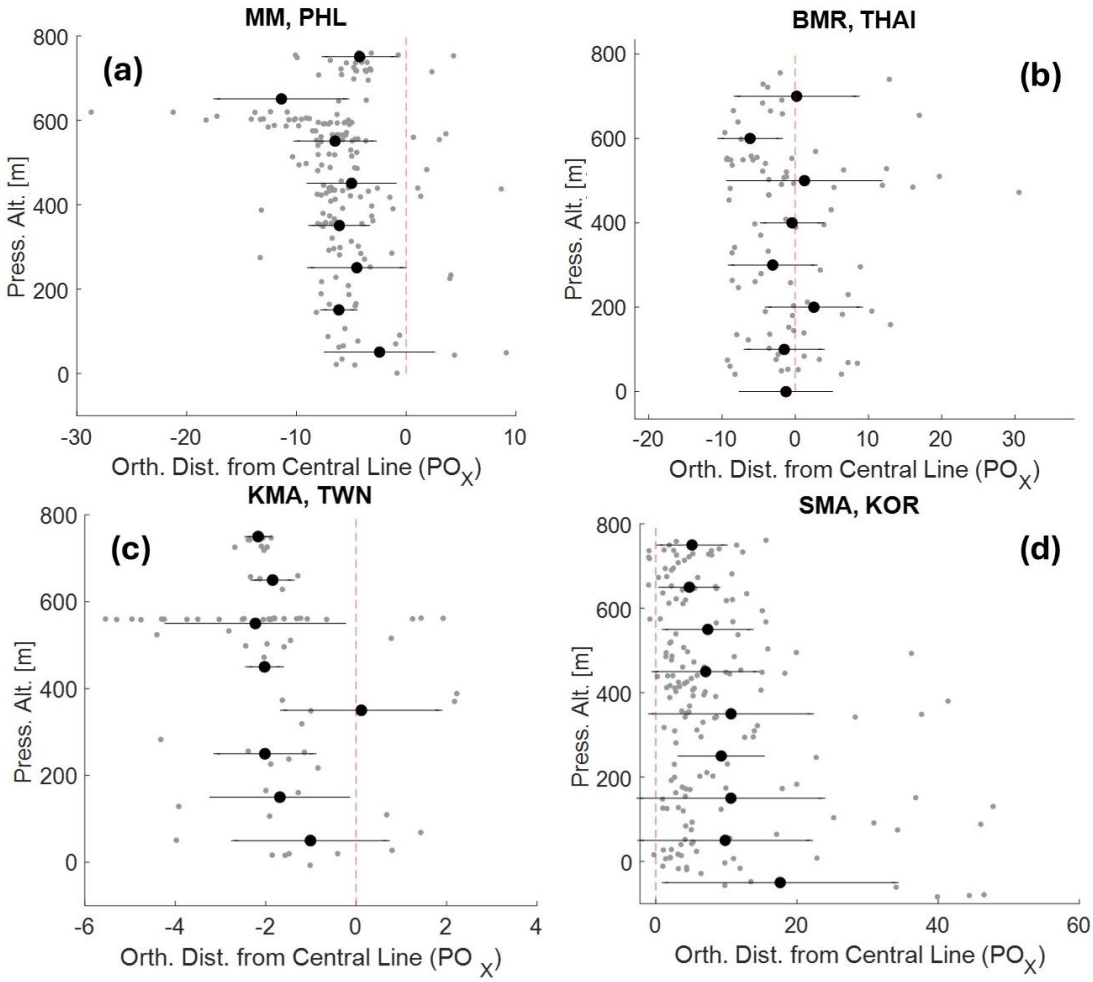

Figure S11. Vertical distributions of PO_x sensitivity, shown as orthogonal distances from the PO_x transition line, for each megacity. Positive values indicate VOC-sensitive conditions, and negative values indicate NO_x-sensitive conditions. The red dashed lines denote the transition line. Grey dots indicate individual data points, and black dots and error bars represent the hourly mean values and standard deviations, respectively.

We extended the orthogonal-distance analysis (Sect. 2.3) to altitudes up to 750 m pressure altitude (asl). Figure S11 shows the vertical distributions of the computed orthogonal distances (Sect. 2.3) in each megacity. Compared with the diurnal distributions (Figs. 4b, 5b, 6b, and 7b), the altitude-binned orthogonal distances show no clear, monotonic tendency with altitude, suggesting that the air masses below 750 m were relatively well mixed. A slight shift toward more positive values near the surface is apparent with elevated NO_x levels near ground (Fig. 2).

S5 Sampling homogeneity

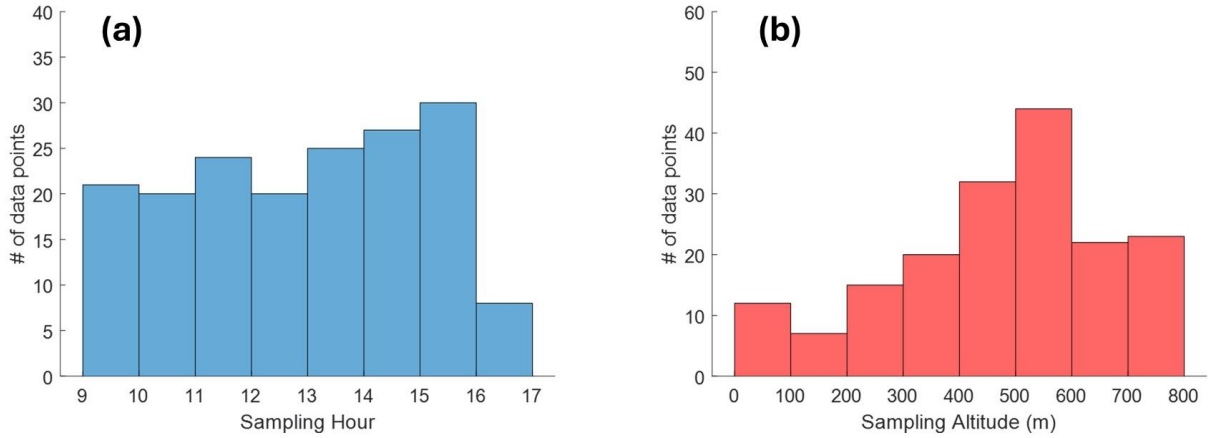

Figure S12. Distributions of (a) sampling hours and (b) altitudes for PO_x sensitivity analysis in MM. The histograms show the number of 1-minute averaged data points.

As noted in the main manuscript (Sect. 4), the temporal and vertical inhomogeneity of airborne sampling can introduce potential biases in the interpretation of ozone production sensitivity across the four studied megacities. Differences in the number and distribution of data points by hour of day and altitude may affect statistical calculations such as regime classification in Table 2 and the modeled impacts of precursor reductions in Fig. 8. Figures S12–S15 illustrate the distributions of 1-minute averaged data points by sampling hour and altitude for each city.

Metro Manila (Fig. S12) shows relatively uniform temporal coverage from 09:00 to 16:00 LT, with a slight drop-off in the late afternoon. According to Fig. 4b, the late afternoon data points generally remain NO_x-sensitive but lie close to transition line. Vertically, data are skewed toward mid-boundary layer altitudes (400–600 m), with fewer measurements below 200 m. Figure S11a indicates that lower-altitude points also tend to cluster near the transition line. Notably, both late afternoon and low-altitude data are associated with elevated NO_x and VOC levels (Figs. 2 and 3), suggesting potentially high PO_x conditions. As a result, this sampling inhomogeneity may lead to an underestimation of data near the transition line under high PO_x conditions, potentially biasing the analysis toward lower sensitivity and underestimating the effects of precursor reductions shown in Fig. 8a.

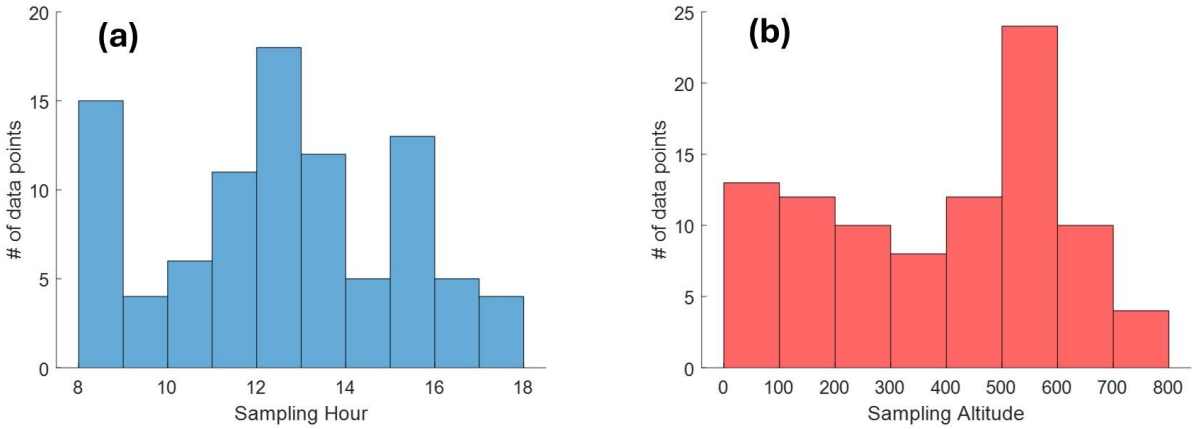

Figure S13. Distributions of (a) sampling hours and (b) altitudes for PO_x sensitivity analysis in BMR. The histograms show the number of 1-minute averaged data points.

Figure S13 shows the distributions of sampling hours and altitudes for the PO_x sensitivity analysis in the Bangkok Metropolitan Region (BMR). While the overall temporal distribution appears uneven, the sampling is relatively homogeneous when divided into broader time blocks (morning and afternoon). One notable limitation is the reduced number of data points after 16:00 LT, which may limit the representation of late-afternoon chemistry. Therefore, the potential influence of VOC-sensitive points in late-afternoon (Fig. 5b) might be underestimated in Table 2 and Fig. 8b. The vertical distribution of orthogonal distances is uniform across altitudes (Fig. S11b), suggesting that vertical sampling inhomogeneity has minimal influence on the sensitivity classification (Table 2) and PO_x reduction estimation (Fig. 8b).

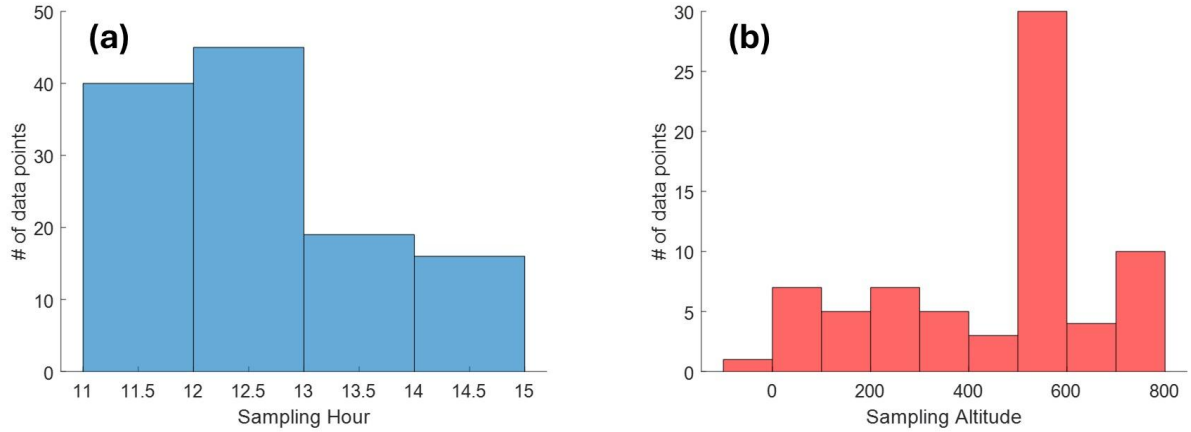

Figure S14. Distributions of (a) sampling hours and (b) altitudes for PO_x sensitivity analysis in TKMA. The histograms show the number of 1-minute averaged data points.

Tainan-Kaohsiung Metropolitan Area (Fig. S14) exhibits the narrowest sampling window among the studied cities, with data collected only between 11:00 and 15:00 LT. As discussed in Sect. 4.1.1, missing early morning sampling may result in an underestimation of the effect of the VOC-sensitive points (Fig. 6) and VOC reduction (Fig. 8c). Vertically, the data are concentrated between 500 m and 600 m. While this altitude range shows a widespread in orthogonal distances (Fig. S11c), the vertical distribution of PO_x sensitivity is generally uniform, except for slightly more VOC-sensitive conditions around 300–400 m. Therefore, the effect of vertical inhomogeneity is expected to be minor.

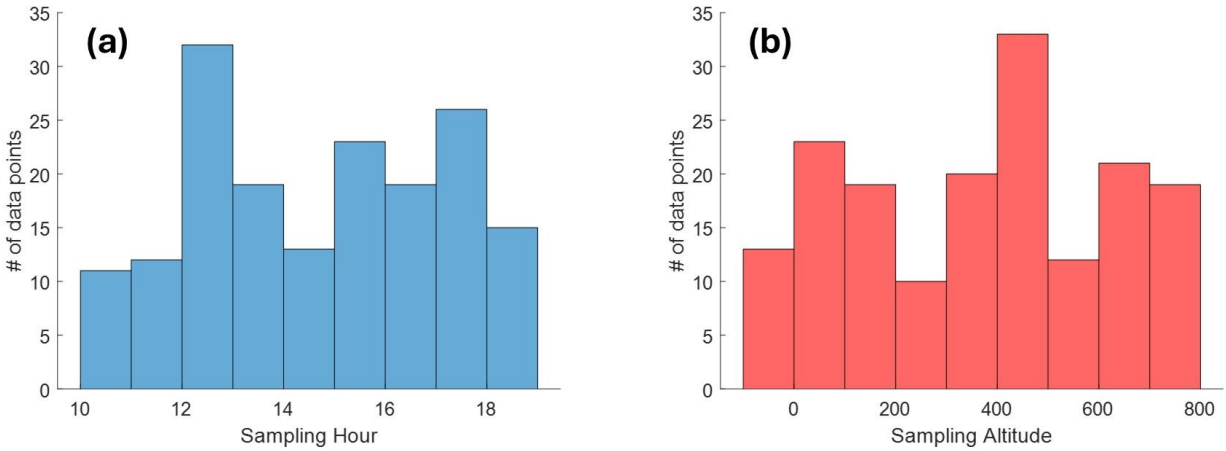

Figure S15. Distributions of (a) sampling hours and (b) altitudes for PO_x sensitivity analysis in SMA. The histograms show the number of 1-minute averaged data points.

The Seoul Metropolitan Area (Fig. S15) shows relatively well-distributed sampling both temporally and vertically. As shown in Fig. S11d, the calculated orthogonal distances remain consistently positive across altitudes. Similarly, Fig. 7b confirms limited diurnal variation in PO_x sensitivity. These patterns suggest that sampling inhomogeneity has minimal impact on the regime classification or PO_x reduction analysis in SMA.

S6 Ozone production sensitivity in SMA during KORUS-AQ

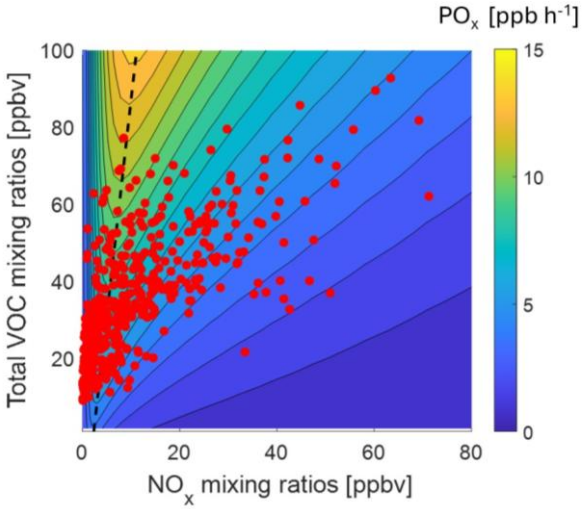

Figure S16. Colored isopleth of ozone production rate (PO_x) as functions of NO_x and VOC mixing ratios in the Seoul Metropolitan Area (SMA) during KORUS-AQ (April–June 2016). The dashed lines denote the transition between NO_x-sensitive (left area of the transition) and VOC-sensitive (right area of the transition) regimes. Red dots indicate the observed data points sampled below 750 m.

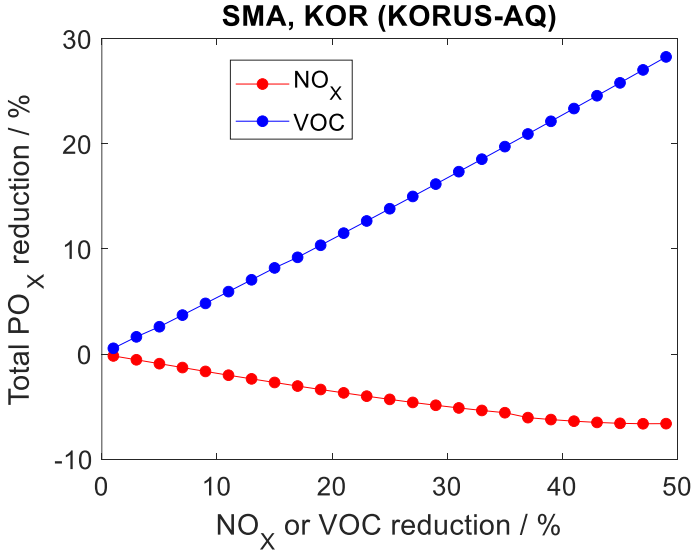

Figure S17. Sensitivity of total PO_x reduction (%) to NO_x and VOC reductions (%) in SMA during KORUS-AQ. Red and blue lines and markers represent the response of PO_x to NO_x and VOC reductions, respectively.

145

Table S4. Fractions of NO_x-sensitive and VOC-sensitive regimes for PO_x in SMA during KORUS-AQ.

Location	Regime	% of Points (All data)	ΣPO_x Contribution (All data)	% of Points (High PO_x[a])	ΣPO_x Contribution (High PO_x[a])
SMA, South Korea (KORUS-AQ)	NO_x-sens.	41%	37%	32%	32%
	VOC-sens.	59%	63%	68%	68%

[a] High PO_x denotes upper 50% of the PO_x distribution (above the median).

150

References

Apel, E. C., Hornbrook, R. S., Hills, A. J., Blake, N. J., Barth, M. C., Weinheimer, A., Cantrell, C., Rutledge, S. A., Basarab, B., Crawford, J., Diskin, G., Homeyer, C. R., Campos, T., Flocke, F., Fried, A., Blake, D. R., Brune, W., Pollack, I., Peischl, J., Ryerson, T., Wennberg, P. O., Crounse, J. D., Wisthaler, A., Mikoviny, T., Huey, G., Heikes, B., O'Sullivan, D., and Riemer, D. D.: Upper tropospheric ozone production from lightning NO_x-impacted convection: Smoke ingestion case study from the DC3 campaign, J. Geophys. Res.- Atmos., 120, 2505–2523, https://doi.org/10.1002/2014JD022121, 2015.

Bailey, S. A., Hannun, R. A., Swanson, A. K., and Hanisco, T. F.: A portable nitrogen dioxide instrument using cavity-enhanced absorption spectroscopy, Atmos. Meas. Tech., 17, 5903–5910, https://doi.org/10.5194/amt-17-5903-2024, 2024.

Brune, W. H., Miller, D. O., Thames, A. B., Brosius, A. L., Barletta, B., Blake, D. R., Blake, N. J., Chen, G., Choi, Y., Crawford, J. H., Digangi, J. P., Diskin, G., Fried, A., Hall, S. R., Hanisco, T. F., Huey, G. L., Hughes, S. C., Kim, M., Meinardi, S., Montzka, D. D., Pusede, S. E., Schroeder, J. R., Teng, A., Tanner, D. J., Ullmann, K., Walega, J., Weinheimer, A., Wisthaler, A., and Wennberg, P. O.: Observations of atmospheric oxidation and ozone production in South Korea, Atmos. Environ., 269, 118854, https://doi.org/10.1016/j.atmosenv.2021.118854, 2022.

Cazorla, M., Wolfe, G. M., Bailey, S. A., Swanson, A. K., Arkinson, H. L., and Hanisco, T. F.: A new airborne laser-induced fluorescence instrument for in situ detection of formaldehyde throughout the troposphere and lower stratosphere, Atmos. Meas. Tech.., 8, 541–552, https://doi.org/10.5194/amt-8-541-2015, 2015.

Crawford, J., Davis, D., Olson, J., Chen, G., Liu, S., Gregory, G., Barrick, J., Sachse, G., Sandholm, S., Heikes, B., Singh, H., and Blake, D.: Assessment of upper tropospheric HO_x sources over the tropical Pacific based on NASA GTE/PEM data: Net effect on HO_x and other photochemical parameters, J. Geophys. Res.-Atmos., 104, 16255–16273, https://doi.org/10.1029/1999JD900106, 1999.

Crounse, J. D., McKinney, K. A., Kwan, A. J., and Wennberg, P. O.: Measurement of Gas-Phase Hydroperoxides by Chemical Ionization Mass Spectrometry, Anal. Chem., 78, 6726–6732, https://doi.org/10.1021/ac0604235, 2006.

Diskin, Glenn S., Podolske, James R., Sachse, Glen William, and Slate, Thomas A.: Open-path airborne tunable diode laser hygrometer, Proc. SPIE, 196–204, https://doi.org/10.1117/12.453736, 2002.

Gaines, S. E., Bowen, S. W., Hipskind, R. S., Bui, T. P., and Chan, K. R.: Comparisons of the NASA ER-2 Meteorological Measurement System with Radar Tracking and Radiosonde Data, J. Atmospheric Ocean. Technol., 9, 210–225, https://doi.org/10.1175/1520-0426(1992)009%253C0210:COTNEM%253E2.0.CO;2, 1992.

Hall, S. R., Ullmann, K., Prather, M. J., Flynn, C. M., Murray, L. T., Fiore, A. M., Correa, G., Strode, S. A., Steenrod, S. D., Lamarque, J.-F., Guth, J., Josse, B., Flemming, J., Huijnen, V., Abraham, N. L., and Archibald, A. T.: Cloud impacts on photochemistry: building a climatology of photolysis rates from the Atmospheric Tomography mission, Atmos Chem Phys, 18, 16809–16828, https://doi.org/10.5194/acp-18-16809-2018, 2018.

Hannun, R. A., Swanson, A. K., Bailey, S. A., Hanisco, T. F., Bui, T. P., Bourgeois, I., Peischl, J., and Ryerson, T. B.: A cavity-enhanced ultraviolet absorption instrument for high-precision, fast-time-response ozone measurements, Atmos. Meas. Tech., 13, 6877–6887, https://doi.org/10.5194/amt-13-6877-2020, 2020.

Jeong, D., Hornbrook, R. S., Hills, A. J., Diskin, G., Halliday, H. S., DiGangi, J. P., Fried, A., Richter, D., Walega, J., Weibring, P., Hanisco, T. F., Wolfe, G. M., St. Clair, J., Peischl, J., Wisthaler, A., Mikoviny, T., Nowak, J. B., Piel, F., Tomsche, L., Holmes, C. D., Soja, A., Gargulinski, E., Crawford, J. H., Dibb, J., Warneke, C., Schwarz, J., and Apel, E. C.: Trace Organic Gas Analyzer Time-of-Flight mass spectrometer (TOGA-TOF) system for airborne observations of formaldehyde, EGUsphere, 2025, 1–34, https://doi.org/10.5194/egusphere-2025-4703, 2025.

Kim, D., Cho, C., Jeong, S., Lee, S., Nault, B. A., Campuzano-Jost, P., Day, D. A., Schroder, J. C., Jimenez, J. L., Volkamer, R., Blake, D. R., Wisthaler, A., Fried, A., DiGangi, J. P., Diskin, G. S., Pusede, S. E., Hall, S. R., Ullmann, K., Huey, L. G., Tanner, D. J., Dibb, J., Knote, C. J., and Min, K.-E.: Field observational constraints on the controllers in glyoxal (CHOCHO) reactive uptake to aerosol, Atmos. Chem. Phys., 22, 805–821, https://doi.org/10.5194/acp-22-805-2022, 2022.

Lee, Y. R., Ji, Y., Tanner, D. J., and Huey, L. G.: A low-activity ion source for measurement of atmospheric gases by chemical ionization mass spectrometry, Atmos. Meas. Tech., 13, 2473–2480, https://doi.org/10.5194/amt-13-2473-2020, 2020.

Min, K.-E., Washenfelder, R. A., Dubé, W. P., Langford, A. O., Edwards, P. M., Zarzana, K. J., Stutz, J., Lu, K., Rohrer, F., Zhang, Y., and Brown, S. S.: A broadband cavity enhanced absorption spectrometer for aircraft measurements of glyoxal, methylglyoxal, nitrous acid, nitrogen dioxide, and water vapor, Atmos. Meas. Tech., 9, 423–440, https://doi.org/10.5194/amt-9-423-2016, 2016.

Nault, B. A., Travis, K. R., Crawford, J. H., Blake, D. R., Campuzano-Jost, P., Cohen, R. C., DiGangi, J. P., Diskin, G. S., Hall, S. R., Huey, L. G., Jimenez, J. L., Min, K.-E., Lee, Y. R., Simpson, I. J., Ullmann, K., and Wisthaler, A.: Using observed urban NO_x sinks to constrain VOC reactivity and the ozone and radical budget in the Seoul Metropolitan Area, Atmos. Chem. Phys., 24, 9573–9595, https://doi.org/10.5194/acp-24-9573-2024, 2024.

Olson, J. R., Crawford, J. H., Chen, G., Brune, W. H., Faloona, I. C., Tan, D., Harder, H., and Martinez, M.: A reevaluation of airborne HO_x observations from NASA field campaigns, J. Geophys. Res.-Atmos., 111, https://doi.org/10.1029/2005JD006617, 2006.

Reinecke, T., Leiminger, M., Jordan, A., Wisthaler, A., and Müller, M.: Ultrahigh Sensitivity PTR-MS Instrument with a Well-Defined Ion Chemistry, Anal. Chem., 95, 11879–11884, https://doi.org/10.1021/acs.analchem.3c02669, 2023.

Ridley, B. A. and Grahek, F. E.: A Small, Low Flow, High Sensitivity Reaction Vessel for NO Chemiluminescence Detectors, J. Atmos. Ocean. Technol., 7, 307–311, https://doi.org/10.1175/1520-0426(1990)007%253C0307:ASLFHS%253E2.0.CO;2, 1990.

Ridley, B. A., Grahek, F. E., and Walega, J. G.: A Small High-Sensitivity, Medium-Response Ozone Detector Suitable for Measurements from Light Aircraft, J. Atmospheric Ocean. Technol., 9, 142–148, https://doi.org/10.1175/1520-0426(1992)009%253C0142:ASHSMR%253E2.0.CO;2, 1992.

Sachse, G. W., Hill, G. F., Wade, L. O., and Perry, M. G.: Fast-response, high-precision carbon monoxide sensor using a tunable diode laser absorption technique, J. Geophys. Res.-Atmos., 92, 2071–2081, https://doi.org/10.1029/JD092iD02p02071, 1987.

Schroeder, J. R., Crawford, J. H., Ahn, J.-Y., Chang, L., Fried, A., Walega, J., Weinheimer, A., Montzka, D. D., Hall, S. R., Ullmann, K., Wisthaler, A., Mikoviny, T., Chen, G., Blake, D. R., Blake, N. J., Hughes, S. C., Meinardi, S., Diskin, G., Digangi, J. P., Choi, Y., Pusede, S. E., Huey, G. L., Tanner, D. J., Kim, M., and Wennberg, P.: Observation-based modeling of ozone chemistry in the Seoul metropolitan area during the Korea-United States Air Quality Study (KORUS-AQ), Elem. Sci. Anthr., 8, 3, https://doi.org/10.1525/elementa.400, 2020.

Simpson, I. J., Blake, D. R., Blake, N. J., Meinardi, S., Barletta, B., Hughes, S. C., Fleming, L. T., Crawford, J. H., Diskin, G. S., Emmons, L. K., Fried, A., Guo, H., Peterson, D. A., Wisthaler, A., Woo, J.-H., Barré, J., Gaubert, B., Kim, J., Kim, M. J., Kim, Y., Knote, C., Mikoviny, T., Pusede, S. E., Schroeder, J. R., Wang, Y., Wennberg, P. O., and Zeng, L.: Characterization, sources and reactivity of volatile organic compounds (VOCs) in Seoul and surrounding regions during KORUS-AQ, Elem. Sci. Anthr., 8, 37, https://doi.org/10.1525/elementa.434, 2020.